Microstructural characterization and mechanical properties of AlMg alloy fabricated by additive friction stir deposition

Zhikang Shen (z45shen@uwaterloo.ca)
University of Waterloo
Mingtao Zhang
Dongxiao Li
Xinyu Liu
Shaolong Chen
Wentao Hou
Yuquan Ding
Zhonggang Sun
Yu Su
Wenya Li
Yanhong Tian

Research Article

Keywords: additive friction stir deposition, 5B70 Al alloy, microstructural characterization, mechanical properties

Posted Date: September 6th, 2022

DOI: https://doi.org/10.21203/rs.3.rs-1998263/v1

Abstract

This work investigates microstructure characterization and mechanical properties of Aluminum alloy fabricated by additive friction stir deposition (AFSD). Microstructure characterize of the Aluminum alloy 5B70 base material (BM) and build were compared using optical microscope (OM) and electron back scattered diffraction (EBSD). Hardness distribution in the direction perpendicular to the cross-section of deposited area was measured and the pattern was evaluated. Tensile tests were performed on the BM and the deposition using digital image correlation (DIC), and the stress distribution states of the specimens were analyzed in real time. After the tensile tests, the fracture micromorphology was characterized using scanning electron microscope (SEM). The results show that a high degree of recrystallization of the grains in the deposition zone occurs and fine equiaxed grains are formed, which are oriented differently. In tensile tests on the deposition, it was found that the strength of the deposition was significantly lower compared to the BM, but its toughness was significantly higher. And there is a significant anisotropy in the mechanical properties of the deposition.

1. Introduction

Additive manufacturing (AM) technology, which could turn 3D models into physical entities, has been extensively investigated in recent years, in which the complex structural parts are fabricated by AM processes via layer-by-layer accumulation of material [1–3]. There are two categories of additive manufacturing technologies, which are fusion-based AM and solid phase AM [4]. The principle of fusion-based AM is using high-energy heat sources under protective gas or vacuum conditions to heat metal materials (including powder, wire, etc.), so that they can be rapidly melted, solidified and stacked layer by layer to form the desired components [5, 6]. Depending on the form of heat source, fusion-based AM technology mainly includes laser AM, electron beam AM and arc AM [7–9]. However, the defects which are internal porosity, local metallurgical defects and thermal cracking of light metal alloys such as aluminum alloys and magnesium alloys occur in the processes of fusion-based AM inevitably. solid phase AM does not generally cause the above-mentioned problems caused by fusion-based AM, because the material does not melt and solidification during the process [10]. The main solid phase AM technologies currently available include ultrasonic additive manufacturing (UAM), cold spray additive manufacturing (CSAM), and friction-based additive manufacturing (FAM) [11–13].

In 2012, Additive Friction Stir Deposition (AFSD) was developed by MELD manufacturing company based on the principle of friction stir welding (FSW). As shown in Fig. 1a hollow and rotating tool head to feed pre-processed metal powder or wire to deposit on the substrate is applied in AFSD. The feed material is softened by the frictional heat of the rotating tool, but the temperature does not reach its melting point. Therefore, the process has advantages that fusion-based AM does not have, such as avoidance of porosity, thermal cracking and ablation of alloying elements [14, 15]. The material undergoes severe plastic deformation and thus generates dynamic recrystallization (DRX) under the action of the tool head, and the rotating tool has a strong stirring effect on the deposited material, promoting the formation of fragmentation and redistribution of the metal particles [16, 17]. In friction stir welding (FSW) and friction

stir spot welding (FSSW), the heat mainly generates from the frictional interaction between the tool shoulder and plastic deformation of the workpiece materials [18–21]. However, the heat generation in AFSD derives from the frictional interaction between the deposited material and the tool shoulder or the substrate. The peak temperature is estimated to be between 0.6 and 0.9 Tm, where Tm is the melting point of the substrate material. Although no melting occurs in the as-deposited material, temperatures are high enough to cause dissolution of strengthening phases in the filler feedstock [22, 23]. Tool rotational speed, tool traversing velocity and feedstock feed rate are the more important parameters in the AFSD process, as they determine the temperatures and material flow patterns, which are critical to the quality of the additive layer [24, 25].

Garcia et al. investigated the heat generation mechanism during AFSD of Cu and Al-Mg-Si alloys. In the deposition zone of Cu, the tool head and the deposited material are in a complete slipping state, so the main heat generation of the Cu deposition layers comes from interfacial friction. For Al-Mg-Si, the interfacial friction is partial slipping, so the heat generation mechanism of Al-Mg-Si deposited layers mainly originated from interfacial friction and volumetric energy dissipation. In AFSD, unlike Cu where the peak temperature T*Peak* is bounded at 49%-79% of the melting point TM, the peak temperature T*Peak* of Al-Mg-Si lies in the range of 76%-92% of the melting point TM. This is due to the fact that the yield strength of Cu decreases more rapidly with increasing of temperature than that of aluminum alloys [26, 27]. For the comparison of Cu and Al-Mg-Si, Griffiths et al. also conducted a detailed investigation, which indicated that a large amount of material rotation was observed in the deposition zone of Al-Mg-Si, which was not present in Cu, and therefore the strain of Al-Mg-Si was higher. Meanwhile, the larger transition zone boundaries were observed in Al-Mg-Si produced more deformation than Cu because the surface area and friction coefficient between Al-Al was higher than that between Cu-Cu [28]. Rivera et al. studied the microstructure of AA2219 deposition using EBSD and found that the average grain size of the deposited material was 2.5 μm, which is much smaller than that of the base material (30 μm), and they also observed that the grain size remained essentially uniform in the deposition direction [29]. Priedeman et al. investigated microstructural evolution in AFSD of Cu with a hardness of 63 HV for the deposition, 62% of the hardness of the base material, which can be attributed to the disappearance of high density dislocations caused by the recrystallization of Cu during the AFSD process. Whereas the reason for the decrease in hardness is in agreement with the literature on FSW of Cu [30, 31]. Phillips investigated role of rotation speed and traversing velocity on the deposition quality of AA6061. Parts fabricated using low feed rates and high traversing speeds produced obvious nibbles and voids due to insufficient material flow. Conversely, when it was fabricated using high feed rates and low traversing speeds, the deposition efficiency was reduced andcharacterized by large amounts of material being pushed out from under the tool face as the form of flash. They also determined the β" precipitates by transmission electron microscopy (TEM) and atom probe tomography (APT) analysis, and thus analyzed the causes of the degradation of the mechanical properties of the deposited AA6061, found that the β" reinforced precipitate was dissolved and then reprecipitated as Mg-Si solute clusters in the deposited material [32]. Perry et al. found that both AA2024 and AA6061 underwent continuous DRX characterized by dynamic recovery, subgrain formation, and strain-induced high angle boundary (HAB) formation. The difference is

that recrystallization is almost complete in AA2024; whereas in AA6061, deformation only causes a portion of the low angle boundaries (LABs) to become high angle boundaries (HABs), resulting in partial recrystallization [33]. Hartley et al. investigated the feasibility of AFSD for solid-state cladding on automotive Al-Mg-Si thin sheet metal (1.4 mm thick). It was found that for thin substrates for automotive use, geometry of the tool determines the cladding quality, and that flat tools are more beneficial to develop good cladding quality. Although the protruding tool facilitates material flow and interfacial bonding, this can easily penetrate the substrate and a thicker deposition layer must be taken to avoid scratching the substrate, which in turn can lead to insufficient deformation of the deposited material to affect the cladding quality [34].

Beck et al. investigated the effect of heat treatment on AFSDed AA6061. ultimate tensile strength of as-deposited (AD) material was reduced by 47% due to dissolution of β. Solutionized/quenched (SQ) showed a 10% reduction in ductility and 58% increase in ultimate tensile strength compared to that of the AD material. Solutionized/quenched/artificially aged (SQA) resulted in regeneration of strength, hardness and β deposition of T6. However, no adverse effect of abnormal grain growth (AGG) on strength and ductility was observed in artificially aged AFSD specimens, thus demonstrating that β precipitation caused by post deposition heat treatment (PDHT) plays a more critical role in determining the strengthening mechanism of AFSDed AA6061 [35]. Griffiths et al. explored the use of AFSD to repair bulk damage in AA7075. It was found that the deposited material was well mixed with the sidewalls of the repaired upper hole or slot. This is a gradual transition from the elongated grains of the AA7075 plate to the fine equiaxed grains of the deposited AA7075 with no visible interface. The lower part of the repaired quality is generally worse than that of the upper part, sometimes showing straight, sharp interfaces separating the elongated grains from the fine, equiaxed grains [36]. Yang simulated the temperature field and stress state of AFSDed Al6061-T6, and the results showed that the heated affected zone presented a bowl-shaped appearance, and the highest temperature reached approximately 78.7% of the melting point at the contact surface between the filled bar and the substrate. As the filler bar moves down, the deposited material on the substrate is extruded to form a deposited layer [37]. Ahmed et al. found that the optimum condition for AFSDed AA2011-T6 of was 1200 rpm and 3–9 mm/min, while the optimum condition for AFSDed AA2011-O was 200 rpm and 1–3 mm/min. In addition, they investigated the effect of alloy temper conditions on the behavior of AFSDed AA2011-T6, and the results indicated that the use of the T6 temper alloy resulted in a lower hardness of additive manufacturing parts (AMPs) than the that in base material, reaching 61% and 51% of the hardness of the base material at 3 and 9 mm/min, respectively. However, the hardness of AMPs fabricated using O temper alloy was higher than that in the starting material and increased by approximately 163% over the hardness of the initial material [38]. AFSD was also applied to fabricate aluminum matrix composites, where fine equiaxed grains were observed, and the deposited material was completely dense with the substrate, no pores can be observed [39–41].

In this work, the first single-layer deposition of AA5B70 was fabricated using the AFSD method. The quality of the first layer deposited is of utmost importance, which determines the reliability of the subsequent deposited layers, since the subsequent deposition process still causes complex thermo-

mechanical coupling effects on the first layer of the build. Therefore, the focus was given to the microstructure and mechanical properties of the first layer of this alloy deposited by the AFSD, and thus on whether usable building blocks could be obtained under this experimental parameter.

2. Experimental Details

AA5B70 was used for both the feedstock and the substrate in the present investigation, whose chemical components and mechanical properties are listed in Tables 1 and 2, respectively. A schematic of the AFSD process is shown in Fig. 1. The feedstock rod was deposited onto the substrate through a hollow and rotating tool (inner diameter 14 mm, outer diameter 28 mm) in this investigation. The AFSD process was performed under load control at a rotating speed of 1500 r/min and a translating speed of 50 mm/min along rolling direction of the substrate. This experiment was performed using a displacement control method, the distance between the tool head and the substrate was constant (1 mm) during the whole AFSD process. Specimens used for performing microstructural examination and hardness tests were cross-sectioned perpendicular to travelling direction using water jet cutting. After that, the specimens were grinded, polished and then etched with Keller's reagent (2 ml HCl + 3 ml HF + 5 ml HNO_3 + 195 ml H_2O) for 240 s, and subsequently observed under optical microscope (OM, OLYMPUS GX71), Electron back scattered diffraction (EBSD, ZEISS Gemini 500) for grain size and recrystallize analysis in the zones of the deposition. Specimen preparation of EBSD analysis consisted of grinding, mechanical polishing, and then followed by electro-polishing with a mixture solution of 10% HNO_3 and 90% C_2H_5OH for 20 s at 15 V and 0 °C. Acquisition of the EBSD data was conducted by ZEISS Gemini 500 field emission (scanning electron microscope) SEM equipped with EBSD attachment.

Table 1
Chemical composition of the investigated alloy (wt.%).

Element	Mg	Mn	Sc	Zr	Ti	Fe	Si	Al
Content	6.15	0.31	0.30	0.15	0.027	0.09	0.068	Bal.

Table 2
Mechanical properties of 5B70 alloy

Tensile strength (MPa)	Yield strength (MPa)	Elongation (%)
440	350	19

Vickers microhardness measurements were conducted at the cross-section of deposition layer under a load of 100 g and a dwell time of 15 s(equipment model is WHVS-1M-AXYZF). Hardness distribution mapping was obtained by measuring the whole cross-section of deposition layer in an interval of 0.5 mm. Location and configuration of the tensile testing specimens was schematically shown in Fig. 2a, whose geometry and dimension were designed according to non-standard tensile specimens (see Fig. 2b). Tensile testing was carried out using in-situ dynamic mechanical test system at room temperature with a cross head speed of 0.5 mm/min. Digital image correlation (DIC, IBTC-5000) technique was used to

investigate the evolution process of local strain distribution on mechanical properties, plastic deformation of specimen. Specimens are sandpapered smooth and then evenly sprayed with white and black lacquer on its surface to ensure accurate image resolution. Specimens after the DIC test are observed by SEM to analyze the fracture pattern of the deposited area and the base material.

3. Results And Discussion

3.1. Microstructure evolution

The whole cross-sectional low magnification map and local high magnification microstructure of the deposition constructed by AFSD are shown in Fig. 3. It can be observed from Fig. 3a that the boundary between the deposition and the substrate can be clearly identified, which presents a wavy appearance, and a serious sink was observed in the center of the deposition. The edge of the deposition is not combined with the substrate, because the material is extruded by the tool head and there is no radial and lateral constraint, and the heat generation in this area is insufficient, but the heat dissipation is fast, which leads to the poor combination of the edge and the substrate. Porosities can be observed in the enlarged view of point A in Fig. 3a, which can be attributed to insufficient heat production at this location. Obvious traces of deposited material flow can be observed in Figs. 3b, e and f, where the material at the edges has a large linear velocity. As shown in Fig. 3f, the material flow process is very complex. An unbound boundary line can be identified in Fig. 3c. The reason for this phenomenon can be attributed to that t the material at the edge has flipped upward under the strong mechanical action of the tool head. Figure 3d shows a high magnification of the central region of the deposition, which shows obvious uniform and fine microstructure [42].

EBSD was applied to investigate details of grain and texture variation of the AFSD deposition and BM specimens. Figures 4a, c, e and g show the inverse pole figures (IPFs) of BM and specific regions of AFSD deposition. The white lines represent low-angle grain boundaries (LAGBs) with the misorientation angle of 2°-15°, and the black lines represent high-angle grain boundaries (HAGBs) with the misorientation angle greater than 15°. Figures 4b, d, f and h show that the $\{100\}$, $\{110\}$, $\{111\}$ pole figures of BM and specific regions of AFSD deposition. The X_0 direction represents the shear direction, and the Y_0 direction represents the shear plane normal. The evolution of the texture is described using the density of pole figures given as multiples of uniform distribution (mud). Figure 5 shows that the average misorientation angles of BM and specific regions of AFSD deposition.

Figure 4a shows that the grains of in BM present an elongated shape, much larger than the grains in the deposited area, and exhibit a more uniform grain orientation, which is related to its roll forming process. As shown in Figs. 4c, e and g, the microstructural changes in the upper and lower middle part of the cross-section of deposition, and the edge of the deposition are obvious, and fine equiaxed grains are observed in these three regions, indicating that DRX occurred during the deposition process, the results of this study are consistent with the findings of previous research [17, 33, 43, 44]. Comparing the EBSD maps of the center top and bottom, the grain size of the former is larger than that of the latter, which may

be due to the higher frictional heat generation between the deposited material and the tool head, while a possibility cannot be ruled out that the top contact with air and the bottom contact with metal, so the heat dissipates more slowly at the top and the top shows grain growth at a higher temperature. Thus, it can be concluded that there is a temperature gradient in the deposition along the build direction. Figure 4g shows the grain characteristics at the edge of the deposited material, where a partial fragmentation of the grains occurred under the strong thermomechanical coupling effect generated by the rotating tool. The grain orientation is more uniform in this region, which is influenced by the rotation of the tool head, which is consistent with the results observed using OM.

As shown in Fig. 4b, the texture in BM exhibits strong consistency, but the maximum texture densities in the three regions of deposition are 2.57, 1.77 and 4.88 respectively (seen as Figs. 4d, f and h), which indicate that the texture is rather weak and random in the middle of the deposition due to the random distribution of DRX grains, this phenomena is consistent with the finding of solder stir zone in FSW [19, 20, 45, 46]. However, the texture density at the edge of the deposition is much higher, indicating the material in this region has a more consistent flow direction under the stirring action of the tool head.

Figure 5 shows the average misorientation angles of the corresponding region in the EBSD diagram, and the ratios of HAGB in the four areas are 11.36%, 58.74%, 69.82% and 44.09%, respectively. This set of data is consistent with the previous results of the IPFs of EBSD, the ratio of HAGB at the bottom is the highest in the center of the deposition, indicating the highest degree of DRX in this region. The degree of DRX at the top is second only to the bottom, but the proportion is also more than half, while the ratio of HAGB at the edge of the deposition is less than half. In addition, the BM has the highest proportion of subcrystals, which accumulate a large number of dislocations during the AFSD processing, while the material undergoes complex thermos-mechanical coupling and the proportion of HAGB is significantly higher.

3.2. Mechanical performance

As a non-heat treatable aluminum alloy, the hardness of 5B70 aluminum alloy is mainly determined by work hardening, whose hardness is affected by plastic deformation and thermal cycling in the AFSD process. Figure 6 shows the hardness distribution of the cross-section of the AFSD build. In general, hardness of the cross-section of build decreases with increasing of heat input, since the DRX causes a significant decrease in dislocation density, which in turn weakens the effect of work hardening. In the thickness direction, however, no significant gradient of hardness distribution can be observed in this direction, since the build is only approximately 1 mm and subjected to only one thermal cycle.

In this work, DIC technique was applied to investigate overall strain history of the specimen under tensile loadings. Real-time photographs were taken of the specimens undergoing load testing throughout the test period. Figure 7 shows the strain distribution states of each sample before, during and after the testing. Figure 7a shows the strain profiles of the base material obtained at different load levels, indicating that the plastic deformation is uniform at the beginning of loading, And this phenomenon is

determined by the uniform microstructure of the BM. As the load increases, the strain is gradually concentrated on one side until fracture. Figures 7b and c show the strain distribution of the specimens in the transverse and longitudinal directions during loading, respectively. It can be observed that the plastic deformation appears to be non-uniform in both directions. Combined with Fig. 7, it can be concluded that non-uniformity of the plasticity of the specimens in the transverse and longitudinal direction can be attributed to the non-uniformity of mechanical properties.

Figure 8 shows stress-strain curves for each specimen. The strength of the AFSD build is lower than that of the base material in both transverse and longitudinal directions, while the toughness of the AFSD build exceeds that of the base material. Table 3 shows the mechanical properties of specimens. The ultimate tensile strength (UTS) of the AFSD build is 350 MPa in the transverse direction, which is 20% lower than that of the BM, and elongation is 22%, which is 16% higher than that of the BM. The UST longitudinal specimen is 276 MPa, which is 37% lower than that of the BM, and the elongation is 27%, which is 42% higher than that of the BM. Combined with Figs. 4 and 5, the deposited material has finer grains and a higher percentage of HAGB, which impede crack extension and improve the material's ability to absorb energy of the fracture process, and thus improving their toughness compared to the BM for both transverse and longitudinal specimens.

As shown in Fig. 9, After the tensile testing, microscopic morphology of the fracture of each specimen was observed by scanning electron microscopy. The microscopic morphology of the fractures of all three specimens shows numerous dimples, while the dimples in Figs. 9b and c are more dense and deeper, indicating that the transverse and longitudinal specimens experienced more severe plastic deformation before failure, whose toughness is betterdue to the fine equiaxed grains formed by recrystallization.

Table 3
Mechanical properties of specimens

	Tensile strength (MPa)	Yield strength (MPa)	Elongation (%)
Transverse	350	260	22
Longitudinal	276	210	27

4. Conclusions

AFSD is an emerging solid-state additive technology. In this work, a layer of aluminum alloy material was successfully deposited on the substrate using this technology, the microstructure and mechanical properties of this deposition were characterized and observed using experimental investigation, and the conclusions are as follows:

1. The interface between the deposition and the substrate shows the shape of wave, porosities are observed in some local areas, and a large number of flashes are generated in this area due to the lack of lateral axial restraint at the edges of the deposition

2. The grains of the BM show an elongated-shaped appearance with a more uniform orientation and a large number of subcrystalline structures due to the rolling process. In the cross-section of the deposition, degree of recrystallization in the central region is high, and the grains are fine, the percentage of HAGB is more than 50%, and the texture orientation is random, while the material in the edge position flows with the rotation of the tool head, and the grains are not uniformly distributed.
3. The hardness in the cross-section of the deposition has a gradient distribution, with a 10% reduction in hardness in the central region compared to that at the edge regions. When tensile tests were performed on both transverse and longitudinal specimens of the deposition, whose strain distribution was found to be non-uniform, indicating the existence of a mechanical property gradient in both directions. In addition, the strength of the transverse and longitudinal specimens decreased by 20% and 37%, respectively, while the elongation increased by 16% and 42%, which can be attributed to the high degree of recrystallization and the high percentage of HAGB in the deposition, which hindered the crack extension and enhanced their toughness. It was found that all specimens showed ductile fracture with the presence of tough nests, while the distribution of dimples in the deposition was more dense and deeper, where the material experienced more intense plastic deformation.

Declarations

Author contribution All authors contributed to the study conception and design. Material preparation, data collection, and analysis were performed by Zhikang Shen and Mingtao Zhang. The first draft was written by Mingtao Zhang, and Zhikang shen made correction. Dongxiao Li did the additive friction stir deposition experiments with the help of Xinyu Liu and Shaolong Chen. Wentao Hou and Zhonggang Sun gave advice for manuscript writing, and Yuquan Ding, Yanhong Tian and Wenya Li guided the analysis All authors read and approved the fnal manuscript.

Competing interests The authors declare no competing interests.

Funding This work was funded by the National Natural Science Foundation of China (No. 51975479, 52174374), Xi'an City Science and Technology Bureau Project (No. 21XJZZ0080), State Key Laboratory of Advanced Welding and Joining, Harbin Institute of Technology (AWJ-23M15), and State Key Laboratory of Solidification Processing (NPU, China) (2021-TZ-01).

References

1. Blakey-Milner B, Gradl P, Snedden G, Brooks M, Pitot J, Lopez E, Leary M, Berto F, Plessis A (2021) ; 209. https://doi.org/10.1016/j.matdes.2021.110008
2. Motallebi R, Savaedi Z, Mirzadeh H (2022) Additive manufacturing – A review of hot deformation behavior and constitutive modeling of flow stress. Curr Opin Solid State Mater Sci 26(3). https://doi.org/10.1016/j.cossms.2022.100992

3. Rathee S, Srivastava M, Pandey PM, Mahawar A, Shukla S (2021) Metal additive manufacturing using friction stir engineering: A review on microstructural evolution, tooling and design strategies. CIRP J Manufact Sci Technol 35:560–588. https://doi.org/10.1016/j.cirpj.2021.08.003
4. Shi L, Li Y, Xiao YC, Wu CS, Liu HJ (2022) Research progress of metal solid phase additive manufacturing based on friction stir. J Mater Eng 50(1):1–14. https://doi.org/10.11868/j.issn.1001-4381.2021.000741
5. Chen H, Sun Y, Yuan W, Pang S, Yan W, Shi Y (2022) A Review on Discrete Element Method Simulation in Laser Powder Bed Fusion Additive Manufacturing. Chin J Mech Engineering: Additive Manuf Front 1(1). https://doi.org/10.1016/j.cjmeam.2022.100017
6. Mostafaei A, Zhao C, He Y, Reza Ghiaasiaan S, Shi B, Shao S, Shamsaei N, Wu Z, Kouraytem N, Sun T, Pauza J, Gordon JV, Webler B, Parab ND, Asherloo M, Guo Q, Chen L, Rollett AD (2022) Defects and anomalies in powder bed fusion metal additive manufacturing. Curr Opin Solid State Mater Sci 26(2). https://doi.org/10.1016/j.cossms.2021.100974
7. Astafurov S, Astafurova E, Reunova K, Melnikov E, Panchenko M, Moskvina V, Maier G, Rubtsov V, Kolubaev E (2021) Electron-beam additive manufacturing of high-nitrogen steel: Microstructure and tensile properties. Mater Sci Engineering: A 826. https://doi.org/10.1016/j.msea.2021.141951
8. Chen H, Sun Y, Yuan W, Pang S, Yan W, Shi Y (2022) A Review on Discrete Element Method Simulation in Laser Powder Bed Fusion Additive Manufacturing. Chin J Mech Engineering: Additive Manuf Front 1(1). https://doi.org/10.1016/j.cjmeam.2022.100017
9. Lin Z, Song K, Yu X (2021) A review on wire and arc additive manufacturing of titanium alloy. J Manuf Process 70:24–45. https://doi.org/10.1016/j.jmapro.2021.08.018
10. Mason CJT, Rodriguez RI, Avery DZ, Phillips BJ, Bernarding BP, Williams MB, Cobbs SD, Jordon JB, Allison PG (2021) Process-structure-property relations for as-deposited solid-state additively manufactured high-strength aluminum alloy. Additive Manuf 40. https://doi.org/10.1016/j.addma.2021.101879
11. James S, Dang C (2020) Investigation of shear failure load in ultrasonic additive manufacturing of 3D CFRP/Ti structures. J Manuf Process 56:1317–1321. https://doi.org/10.1016/j.jmapro.2020.04.026
12. Ren Y, Tariq NuH, Liu H, Zhao L, Cui X, Shen Y, Wang J, Xiong T (2021) Study of microstructural and mechanical anisotropy of 7075 Al deposits fabricated by cold spray additive manufacturing. Mater Design 212. https://doi.org/10.1016/j.matdes.2021.110271
13. Kumar Srivastava A, Kumar N, Rai Dixit A (2021) Friction stir additive manufacturing – An innovative tool to enhance mechanical and microstructural properties. Mater Sci Engineering: B 263. https://doi.org/10.1016/j.mseb.2020.114832
14. Gopan V, Leo Dev Wins K, Surendran A (2021) Innovative potential of additive friction stir deposition among current laser based metal additive manufacturing processes: A review. CIRP J Manufact Sci Technol 32:228–248. https://doi.org/10.1016/j.cirpj.2020.12.004

15. Yu HZ, Mishra RS (2020) Additive friction stir deposition: a deformation processing route to metal additive manufacturing. Mater Res Lett 9(2):71–83. https://doi.org/10.1080/21663831.2020.1847211
16. Elfishawy E, Ahmed MMZ, El-Sayed Seleman MM (2020) Additive Manufacturing of Aluminum Using Friction Stir Deposition. TMS 2020 149th Annual Meeting & Exhibition Supplemental Proceedings: 227 – 38. /Elfishawy E, Ahmed MMZ and El-Sayed Seleman MM (2020). Additive Manufacturing of Aluminum Using Friction Stir Deposition. TMS 2020 149th Annual Meeting & Exhibition Supplemental Proceedings: 227 – 38. https://doi.org/10.1007/978-3-030-36296-6_21
17. Rivera OG, Allison PG, Jordon JB, Rodriguez OL, Brewer LN, McClelland Z, Whittington WR, Francis D, Su J, Martens RL, Hardwick N (2017) Microstructures and mechanical behavior of Inconel 625 fabricated by solid-state additive manufacturing. Mater Sci Engineering: A 694:1–9. https://doi.org/10.1016/j.msea.2017.03.105
18. Nasiri AM, Shen Z, Hou JSC, Gerlich AP (2018) Failure analysis of tool used in refill friction stir spot welding of Al 2099 alloy. Eng Fail Anal 84:25–33. https://doi.org/10.1016/j.engfailanal.2017.09.009
19. Ni Y, Fu L, Shen Z, Liu XC (2019) Role of tool design on thermal cycling and mechanical properties of a high-speed micro friction stir welded 7075-T6 aluminum alloy. J Manuf Process 48:145–153. https://doi.org/10.1016/j.jmapro.2019.10.025
20. Shen Z, Li WY, Ding Y, Hou W, Liu XC, Guo W, Chen HY, Liu X, Yang J, Gerlich AP (2022) Material flow during refill friction stir spot welded dissimilar Al alloys using a grooved tool. J Manuf Process 49:260–270. https://doi.org/10.1016/j.jmapro.2019.11.029
21. Zhao H, Shen Z, Booth M, Wen J, Fu L, Gerlich AP (2018) Calculation of welding tool pin width for friction stir welding of thin overlapping sheets. Int J Adv Manuf Technol 98(5–8):1721–1731. https://doi.org/10.1007/s00170-018-2350-x
22. Stubblefield GG, Fraser K, Phillips BJ, Jordon JB, Allison PG (2021) A meshfree computational framework for the numerical simulation of the solid-state additive manufacturing process, additive friction stir-deposition (AFS-D). Mater Design 202. https://doi.org/10.1016/j.matdes.2021.109514
23. Mishra RS, Ma ZY (2005) Friction stir welding and processing. Mater Sci Engineering: R: Rep 50(1–2):1–78. https://doi.org/10.1016/j.mser.2005.07.001
24. Anderson-Wedge K, Avery DZ, Daniewicz SR, Sowards JW, Allison PG, Jordon JB, Amaro RL (2021) Characterization of the fatigue behavior of additive friction stir-deposition AA2219. Int J Fatigue 142. https://doi.org/10.1016/j.ijfatigue.2020.105951
25. Joshi SS, Patil SM, Mazumder S, Sharma S, Riley DA, Dowden S, Banerjee R, Dahotre NB (2022) Additive friction stir deposition of AZ31B magnesium alloy. J Magnesium Alloys. https://doi.org/10.1016/j.jma.2022.03.011
26. Garcia D, Hartley WD, Rauch HA, Griffiths RJ, Wang R, Kong ZJ, Zhu Y, Yu HZ (2020) In situ investigation into temperature evolution and heat generation during additive friction stir deposition: A comparative study of Cu and Al-Mg-Si. Additive Manuf 34. https://doi.org/10.1016/j.addma.2020.101386

27. Mironov S, Inagaki K, Sato YS, Kokawa H (2015) Microstructural evolution of pure copper during friction-stir welding. Phil Mag 95(4):367–381. https://doi.org/10.1080/14786435.2015.1006293
28. Griffiths RJ, Garcia D, Song J, Vasudevan VK, Steiner MA, Cai W, Yu HZ (2021) Solid-state additive manufacturing of aluminum and copper using additive friction stir deposition: Process-microstructure linkages. Materialia 15. https://doi.org/10.1016/j.mtla.2020.100967
29. Rivera OG, Allison PG, Brewer LN, Rodriguez OL, Jordon JB, Liu T, Whittington WR, Martens RL, McClelland Z, Mason CJT, Garcia L, Su JQ, Hardwick N (2018) Influence of texture and grain refinement on the mechanical behavior of AA2219 fabricated by high shear solid state material deposition. Mater Sci Engineering: A 724:547–558. https://doi.org/10.1016/j.msea.2018.03.088
30. Priedeman JL, Phillips BJ, Lopez JJ, Tucker Roper BE, Hornbuckle BC, Darling KA, Jordon JB, Allison PG, Thompson GB (2020) Microstructure Development in Additive Friction Stir-Deposited Cu. Metals 10(11). https://doi.org/10.3390/met10111538
31. Lee W-B, Jung S-B (2004) The joint properties of copper by friction stir welding. Mater Lett 58(6):1041–1046. https://doi.org/10.1016/j.matlet.2003.08.014
32. Phillips BJ, Avery DZ, Liu T, Rodriguez OL, Mason CJT, Jordon JB, Brewer LN, Allison PG Microstructure-deformation relationship of additive friction stir-deposition Al–Mg–Si. Materialia 2019;7. https://doi.org/10.1016/j.mtla.2019.100387
33. Perry MEJ, Griffiths RJ, Garcia D, Sietins JM, Zhu Y, Yu HZ (2020) Morphological and microstructural investigation of the non-planar interface formed in solid-state metal additive manufacturing by additive friction stir deposition. Additive Manuf 35. https://doi.org/10.1016/j.addma.2020.101293
34. Hartley WD, Garcia D, Yoder JK, Poczatek E, Forsmark JH, Luckey SG, Dillard DA, Yu HZ (2021) Solid-state cladding on thin automotive sheet metals enabled by additive friction stir deposition. J Mater Process Technol 291. https://doi.org/10.1016/j.jmatprotec.2021.117045
35. Beck SC, Rutherford BA, Avery DZ, Phillips BJ, Rao H, Rekha MY, Brewer LN, Allison PG, Jordon JB (2021) The effect of solutionizing and artificial aging on the microstructure and mechanical properties in solid-state additive manufacturing of precipitation hardened Al–Mg–Si alloy. Mater Sci Engineering: A 819. https://doi.org/10.1016/j.msea.2021.141351
36. Griffiths RJ, Petersen DT, Garcia D, Yu HZ (2019) Additive Friction Stir-Enabled Solid-State Additive Manufacturing for the Repair of 7075 Aluminum Alloy. Appl Sci 9(17). https://doi.org/10.3390/app9173486
37. Yang HG (2020) Numerical Simulation of the Temperature and Stress State on the Additive Friction Stir with the Smoothed Particle Hydrodynamics Method. Strength Mater 52(1):24–31. https://doi.org/10.1007/s11223-020-00146-1
38. Ahmed MMZ, El-Sayed Seleman MM, Elfishawy E, Alzahrani B, Touileb K, Habba MIA (2021) The Effect of Temper Condition and Feeding Speed on the Additive Manufacturing of AA2011 Parts Using Friction Stir Deposition. Mater (Basel) 14(21). https://doi.org/10.3390/ma14216396
39. Griffiths RJ, Perry MEJ, Sietins JM, Zhu Y, Hardwick N, Cox CD, Rauch HA, Yu HZ (2018) A Perspective on Solid-State Additive Manufacturing of Aluminum Matrix Composites Using MELD. J

Mater Eng Perform 28(2):648–656. https://doi.org/10.1007/s11665-018-3649-3

40. Phillips BJ, Williamson CJ, Kinser RP, Jordon JB, Doherty KJ, Allison PG (2021) Microstructural and Mechanical Characterization of Additive Friction Stir-Deposition of Aluminum Alloy 5083 Effect of Lubrication on Material Anisotropy. Mater (Basel) 14(21). https://doi.org/10.3390/ma14216732
41. Yu HZ, Jones ME, Brady GW, Griffiths RJ, Garcia D, Rauch HA, Cox CD, Hardwick N (2018) Non-beam-based metal additive manufacturing enabled by additive friction stir deposition. Scripta Mater 153:122–130. https://doi.org/10.1016/j.scriptamat.2018.03.025
42. McNelley TR, Swaminathan S, Su JQ (2008) Recrystallization mechanisms during friction stir welding/processing of aluminum alloys. Scripta Mater 58(5):349–354. https://doi.org/10.1016/j.scriptamat.2007.09.064
43. Hartley WD, Garcia D, Yoder JK, Poczatek E, Forsmark JH, Luckey SG, Dillard DA, Yu HZ (2021) Solid-state cladding on thin automotive sheet metals enabled by additive friction stir deposition. J Mater Process Technol 291. https://doi.org/10.1016/j.jmatprotec.2021.117045
44. McNelley TR, Swaminathan S, Su JQ (2008) Recrystallization mechanisms during friction stir welding/processing of aluminum alloys. Scripta Mater 58(5):349–354. https://doi.org/10.1016/j.scriptamat.2007.09.064
45. Ding T, Yan HJ, Chen JH, Xia WJ, Su B (2021) Effect of welding speed on microstructure and mechanical properties of Al – Mg – Mn – Zr – Tialloy sheet during friction stir welding. Trans Nonferrous Met Soc China 31(12):3626–3642. .https://doi.org/10.1016/S1003-6326(21)65753-9
46. Hou W, Ding Y, Huang G, Huda N, Shah LHA, Piao Z, Shen Y, Shen Z, Gerlich A (2022) The role of pin eccentricity in friction stir welding of Al-Mg-Si alloy sheets: microstructural evolution and mechanical properties. Int J Adv Manuf Technol. https://doi.org/10.1007/s00170-022-09793-x

Figures

Figure 1

Schematic illustrations of additive friction stir deposition (AFSD) process

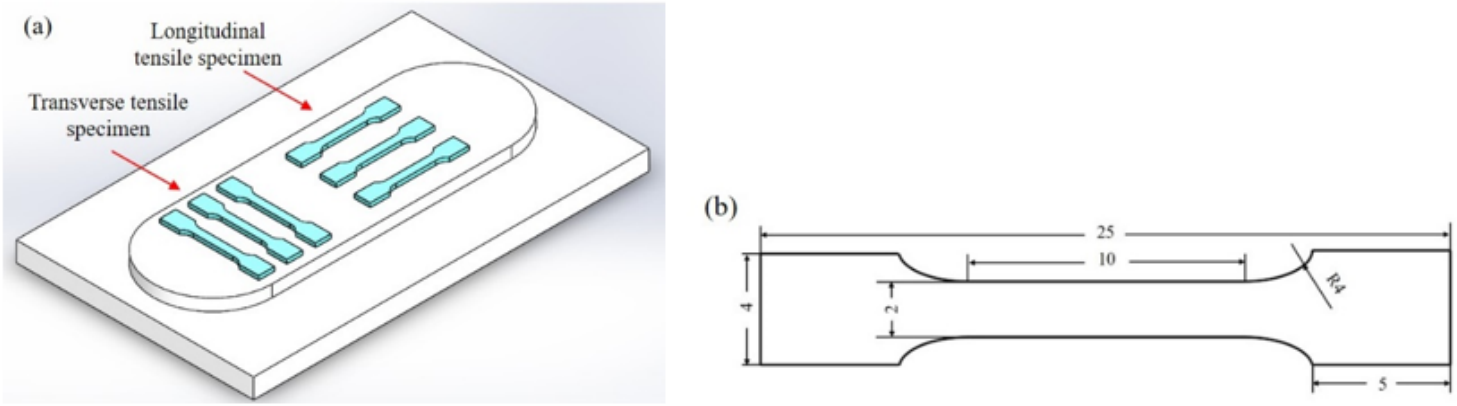

Figure 2

(a) Schematic illustration of the location and configuration of the specimens; (b) Geometry and dimension of tensile specimen

Figure 3

Optical micrographs of deposition: (a) cross-section of deposition and substrate; (b) zone B; (c) zone C; (d) zone D; (e) zone E; (f) zone F

Figure 4

IPFs and PFs of specimens: (a) IPF of BM; (b) PF of BM; (c) IPF of upper middle part of the cross-section of deposition; (d) PF of upper middle part of the cross-section of deposition; (e) IPF of lower middle part of the cross-section of deposition; (f) PF of lower middle part of the cross-section of deposition; (g) IPF of the edge of the cross-section of deposition; (h) PF of the edge of the cross-section of deposition

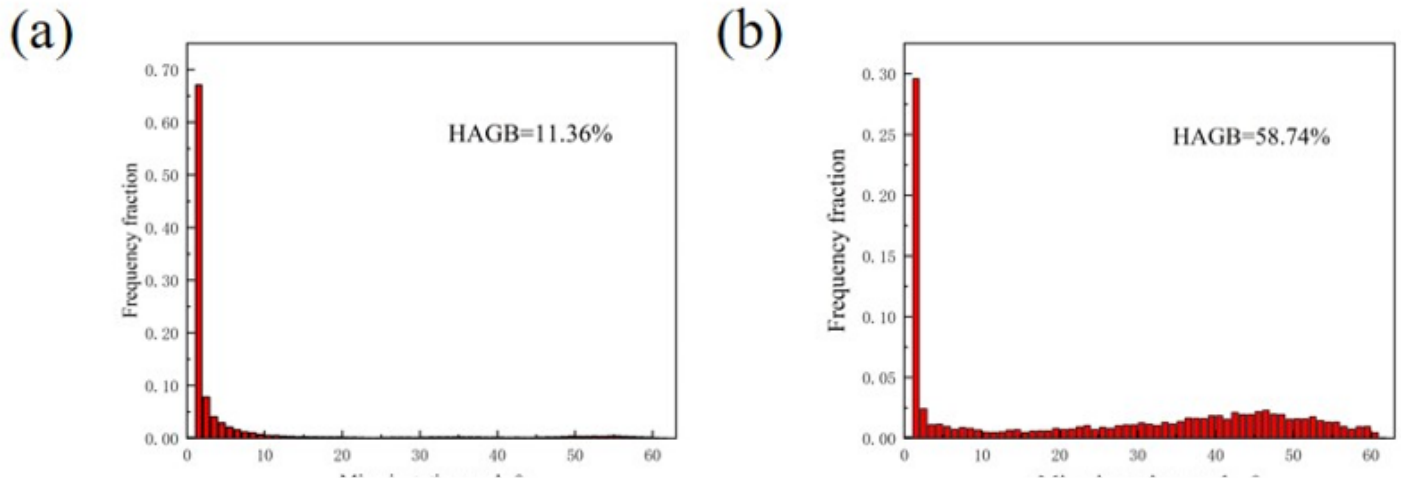

Figure 5

The misorientation angle of specimens: (a) BM; (b) Upper middle part of the cross-section of deposition; (c) Lower middle part of the cross-section of deposition; (d) the edge of the cross-section of deposition

Figure 6

Microhardness nephogram of the component

Figure 7

The strain state of specimens in successive loading: (a) BM; (b) transverse specimen; (c) longitudinal specimen

Figure 8

The stress-strain curve of the specimens

Figure 9

Fracture surface of specimens: (a) BM; (b) transverse specimen; (c) longitudinal specimen